

Topological quantum fluctuations and travelling wave amplifiers

Vittorio Peano,¹ Martin Houde,² Florian Marquardt,^{1,3} and Aashish A. Clerk²

¹*Institute for Theoretical Physics, University of Erlangen-Nürnberg, Staudtstr. 7, 91058 Erlangen, Germany*

²*Department of Physics, McGill University, 3600 rue University, Montreal, Quebec, H3A 2T8, Canada*

³*Max Planck Institute for the Science of Light, Günther-Scharowsky-Straße 1/Bau 24, 91058 Erlangen, Germany*

(Dated: April 25, 2016)

It is now well-established that photonic systems can exhibit topological energy bands; similar to their electronic counterparts, this leads to the formation of chiral edge modes which can be used to transmit light in a manner that is protected against back-scattering. While it is understood how classical signals can propagate under these conditions, it is an outstanding important question how the quantum vacuum fluctuations of the electromagnetic field get modified in the presence of a topological band structure. We address this challenge by exploring a setting where a non-zero topological invariant guarantees the presence of a parametrically-unstable chiral edge mode in a system with boundaries, even though there are no bulk-mode instabilities. We show that one can exploit this to realize a topologically protected, quantum-limited travelling-wave parametric amplifier. The device is naturally protected both against internal losses and back-scattering; the latter feature is in stark contrast to standard travelling wave amplifiers. This adds a new example to the list of potential quantum devices that profit from topological transport.

The quantization of the electromagnetic field introduces a fundamentally new phenomenon into physics: vacuum fluctuations that permeate all of space. These fluctuations were initially seen as a basic unalterable feature of space-time, before it was realized that they could be engineered to great effect. Simply modifying geometric boundary conditions changes the size of the fluctuations as a function of position and frequency, leading to phenomena such as the Purcell enhancement of spontaneous emission. The introduction of nonlinear optical materials gives rise to an even greater level of control, leading to the possibility of squeezed vacuum states [1], with important applications to sensing beyond the limits usually set by quantum mechanics [2–4].

In recent years, new approaches for altering the dynamics of wave fields have gained prominence, based on engineering periodic materials to elicit topological properties. Topologically protected unidirectional wave propagation was originally discovered in the study of 2D electrons in strong magnetic fields, and underlies the robust quantization of the Hall conductance [5]. The engineering of topological photonic materials has been the focus of intense theoretical investigation [6], and various experimental platforms have already been developed [7–10]. Phononic topological states have also attracted recent attention [11–15] and the first experimental steps at the macroscopic scale have been taken [15–17].

Despite this considerable work in topological photonics and phononics, using topology to address the engineering of vacuum fluctuations has not been addressed. Most photonic and phononic topological systems are based on a single particle Hamiltonian which conserves particle number. These topological states mimic well known electronic topological phases such as the Quantum Hall phase [7, 13, 18–25], or the spin Hall phase [10, 16, 26–28] and have a trivial vacuum. In order to modify the properties of the vacuum one has to introduce particle non-conserving terms to the Hamiltonian which can coher-

ently add and remove pairs of particles from the system; these terms have a formal similarity to pairing terms in the mean-field description of a fermionic superconductor. If the amplitude of these terms is sufficiently weak, the system remains stable; even in this regime, the bosonic nature of the particles makes the topological properties of such Hamiltonians very different from their fermionic (topological superconductor) counterparts [29–32]. An even starker difference occurs when the parametric terms lead to dynamical instabilities [33, 34]. These instabilities have no fermionic analogue, and are akin to the parametric instability in an oscillator whose spring constant is modulated in time.

Here, we consider a situation where parametric driving is introduced to a system where photons hop on a lattice in the presence of a synthetic gauge field (see Fig. 1a). We show how to realize an exotic situation where all bulk modes are stable, but where the topologically-protected chiral edge modes that exist in a system with a boundary are unstable. This leads to an unusual spatially-dependent modification of vacuum fluctuations: when the system is stabilized by dissipation, quantum fluctuations in the bulk are only weakly perturbed, whereas those along the system edge are strongly distorted. The result is not just an unusual driven-dissipative quantum state, but also a unique kind of photonic device: as we show in detail, the system serves both as a topologically-protected, non-reciprocal, quantum-limited amplifier, as well as a source of chiral squeezed light. It thus represents a potentially powerful new kind of application of topological materials.

I. IDENTIFYING UNSTABLE MODES

Before delving into the details of our proposal, it is useful to discuss the underlying theoretical ideas in a general setting. Our main goal is to exploit topological features of a dynamically unstable Hamiltonian, adding dissipation

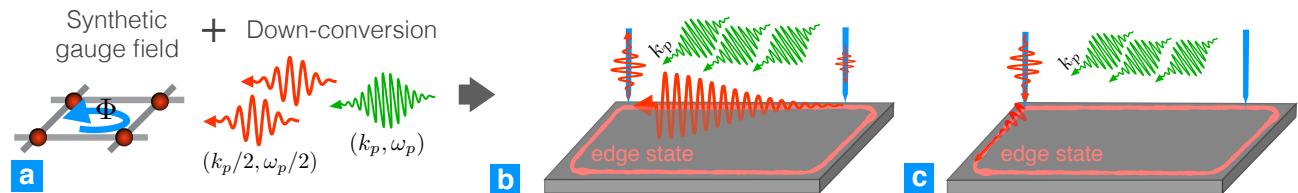


Figure 1. Set up figure: (a) Scheme of the basic interactions: (i) Photons hopping anti-clockwise around a plaquette pick up a phase Φ that can be interpreted as a synthetic gauge field flux. (ii) Pump photons with frequency ω_p and quasimomentum k_p are down-converted into a photon pair with frequency $\omega_p/2$ and quasimomentum $k_p/2$. (b-c) Combining the two interactions in a finite geometry allows to engineer a topologically protected quantum-limited amplifier. A signal injected into the device via a tapered fiber propagates unidirectionally along the edge. (b) With the appropriate choice of pump frequency ω_p and quasimomentum k_p , the signal is amplified while it travels along the upper edge. A second tapered fiber detects the amplified signal. (c) When the input and the output fiber are exchanged the signal propagates along a different path where it decays due to the lack of phase matching. This leads to non-reciprocal amplification.

to realize a non-thermal steady state. In the absence of topological considerations, this is a situation that is ubiquitous in quantum optics. The simplest bosonic Hamiltonian exhibiting instability is the single-mode squeezing Hamiltonian:

$$\hat{H}_S = \Delta \hat{a}^\dagger \hat{a} + \frac{i}{2} \nu (\hat{a}^\dagger \hat{a}^\dagger - \hat{a} \hat{a}), \quad (1)$$

where \hat{a} is a bosonic annihilation operator. Heuristically, \hat{H}_S describes photons in a single cavity mode (effective energy Δ) which are subject to coherent two-particle driving (with amplitude ν). Without dissipation, \hat{H}_S becomes unstable and cannot be diagonalized when the driving amplitude exceeds the energy cost for creating a pair of photons, i.e. when $\nu > |\Delta|$. In this regime, the dynamics corresponds to an ever-growing, exponential accumulation of entangled pairs of bosonic particles: there is no stationary state.

If we now add dissipation, stability can be restored by offsetting the effective two-particle driving described by \hat{H}_S against the decay rate κ of the mode; one requires $\kappa > 2\sqrt{\nu^2 - \Delta^2}$. The result is a non-thermal stationary state having a steady flux of excitations flowing from the driven mode to the dissipative bath (which could be a waveguide serving as an input-output port). This is precisely the situation realized in a standard parametric amplifier: the linear-response properties of this driven-dissipative steady-state allow for quantum-limited amplification of an additional signal drive. The required two-photon driving in Eq.(1) is generically realized by using a nonlinearity and parametric down-conversion of a driven pump mode.

With these preliminaries, we now consider a very general quadratic Hamiltonian describing bosons on a lattice subject to parametric driving:

$$\hat{H} = \sum_{\mathbf{k}ss'} \hat{a}_{\mathbf{k},s}^\dagger \nu_{\mathbf{k}ss'} \hat{a}_{\mathbf{k},s'} + \frac{i}{2} \left(\hat{a}_{\mathbf{k},s}^\dagger \nu_{\mathbf{k}ss'} \hat{a}_{\mathbf{k}_p - \mathbf{k},s'} - h.c. \right). \quad (2)$$

Here the ladder operator $\hat{a}_{\mathbf{k},s}$ annihilates a boson with quasimomentum \mathbf{k} in the state s , where $s, s' = 1, \dots, N$

label polarization and/or sublattice degrees of freedom. The first set of terms describes the hopping of photons on the lattice, and explicitly conserves both particle number and quasimomentum. It could be diagonalized to yield a standard band structure: for each quasimomentum \mathbf{k} , we would have N band eigenstates. The second set of parametric driving terms break particle number conservation, and in general also break the conservation of quasimomentum: the two-photon driving injects pairs with a net quasimomentum \mathbf{k}_p , implying that quasimomentum is only conserved modulo \mathbf{k}_p . For a realization based on a driven $\chi^{(2)}$ medium, the two-photon driving terms correspond to the down-conversion of pump photons with quasimomentum \mathbf{k}_p into a pair of photons with quasimomenta \mathbf{k} and $\mathbf{k}_p - \mathbf{k}$, respectively. Having a non-zero quasimomentum for injected pairs will be a crucial resource when we attempt to control parametric instabilities.

Analogous to the simple Hamiltonian in Eq.(1), the lattice Hamiltonian in Eq. (2) exhibits instabilities when the amplitude for creating a pair of photons exceeds the energy of the pair. Formally, one can introduce a generalized normal mode decomposition of this generic Hamiltonian which explicitly separates out stable modes and unstable modes. One obtains [see Appendix A]:

$$\hat{H} = \sum_{\mathbf{k}} \sum_{n \in S_{\mathbf{k}}} E_{n,\mathbf{k}} \hat{n}_{n,\mathbf{k}} + \frac{1}{2} \sum_{n \in U_{\mathbf{k}}} \hat{H}_{n,\mathbf{k}}. \quad (3)$$

For each quasimomentum \mathbf{k} in the first Brillouin zone, we will now have both a set of stable modes (indexed by $n \in S_{\mathbf{k}}$), and a set of unstable modes ($n \in U_{\mathbf{k}}$). The first n -sum in Eq.(3) describes the stable modes: they are described by canonical bosonic annihilation operators $\hat{\beta}_{n,\mathbf{k}}$, and enter the Hamiltonian in the standard manner, as a real energy times a number operator $\hat{n}_{n,\mathbf{k}} = \hat{\beta}_{n,\mathbf{k}}^\dagger \hat{\beta}_{n,\mathbf{k}}$. The unstable modes can also be described by canonical bosonic annihilation operators $\hat{\beta}_{n,\mathbf{k}}$. They however enter the Hamiltonian via unstable two-mode squeezing (parametric amplifier) Hamiltonians:

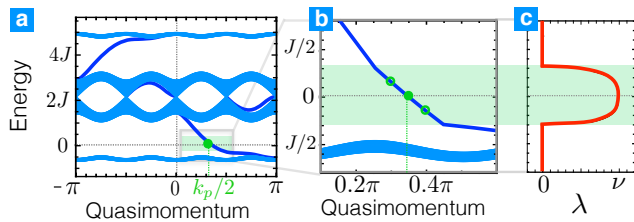


Figure 2. Topological Band structure. (a) Band structure of a semi-infinite strip for the Hofstadter model with a flux of $\pi/2$ (when the parametric driving is switched off). The edge states are plotted in dark blue. The energy is counted off from half of the pump photon energy. The solid green circle indicates the tuning of the pump photon quasimomentum k_p required to resonantly excite pairs of down-converted edge state photons with quasimomentum $k_p/2$ (at the quasimomentum $k_p/2$ the edge state should have energy $E = 0$). (b) Zoom of the band structure for a finite laser power. In the unstable energy interval highlighted in green, pairs of Bogoliubov excitations having quasimomenta $k_p/2 \pm \delta k$ are also excited. The corresponding amplification amplitude λ is shown in panel (c) [Parameters: $\omega_0 = 2.15J$, $\Phi = \pi/2$, $k_p = 2.2$. In (b-c) $\nu = 0.08J$]

$$\hat{H}_{n,\mathbf{k}} = E_{n,\mathbf{k}}(\hat{n}_{n,\mathbf{k}} - \hat{n}_{n,\mathbf{k}_p - \mathbf{k}}) + i\lambda_{n,\mathbf{k}} \left(\hat{\beta}_{n,\mathbf{k}}^\dagger \hat{\beta}_{n,\mathbf{k}_p - \mathbf{k}}^\dagger - h.c. \right), \quad (4)$$

where $E_{n,\mathbf{k}} = -E_{n,\mathbf{k}_p - \mathbf{k}}$ and $\lambda_{n,\mathbf{k}} = \lambda_{n,\mathbf{k}_p - \mathbf{k}}$ are both real. This effective Hamiltonian for the unstable modes has a simple interpretation: pairs of quasiparticles with opposite energies $\pm E_{n,\mathbf{k}}$ are created with an amplitude $\lambda_{n,\mathbf{k}}$. We stress that for any non-zero $\lambda_{n,\mathbf{k}}$, $\hat{H}_{n,\mathbf{k}}$ is unstable (as the total energy for creating the relevant pair of excitations is always zero). The quasiparticle operators $\hat{\beta}_{n,\mathbf{k}}^\dagger$ in Eqs.(3,4) are a complete set of Bogoliubov ladder operators.

II. PARAMETRICALLY DRIVEN HOFSTADTER MODEL

Having established the necessary theoretical framework, we will now show how to engineer a Hamiltonian whose only unstable Bogoliubov modes $\hat{\beta}_{n,\mathbf{k}}^\dagger$ are chiral states co-propagating along the physical boundary of a topological system. We consider photons hopping on a 2D square lattice in the presence of a synthetic magnetic field flux, which are also subject to parametric two-photon driving on each site (see Fig. 1(c)). Writing the Hamiltonian in the position basis, we have

$$\hat{H} = \sum_{\mathbf{j}} \omega_{\mathbf{j}} \hat{a}_{\mathbf{j}}^\dagger \hat{a}_{\mathbf{j}} - \sum_{\langle \mathbf{i}, \mathbf{j} \rangle} J_{\mathbf{i}\mathbf{j}} \hat{a}_{\mathbf{i}}^\dagger \hat{a}_{\mathbf{j}} + \frac{i}{2} \nu \sum_{\mathbf{j}} \left(e^{i\theta_{\mathbf{j}}} \hat{a}_{\mathbf{j}}^\dagger \hat{a}_{\mathbf{j}}^\dagger - h.c. \right), \quad (5)$$

where $\hat{a}_{\mathbf{j}}$ is the photon annihilation operator on site $\mathbf{j} = (j_x, j_y)$, and $\omega_{\mathbf{j}}$ are the corresponding onsite energies. As

usual, the synthetic gauge field is encoded in the pattern of phases $\phi_{\mathbf{i}\mathbf{j}}$ of the nearest-neighbor hopping rates, $J_{\mathbf{i}\mathbf{j}} = J \exp(i\phi_{\mathbf{i}\mathbf{j}})$. We take the synthetic flux per plaquette to be $\Phi = \pi/2$. Working in the Landau gauge, we then have $\phi_{\mathbf{i}\mathbf{j}} = 0$ for vertical hopping and $\phi_{\mathbf{i}\mathbf{j}} = -\pi j_y/2$ for rightwards hopping. The parametric driving amplitude on a given site \mathbf{j} is written $\nu e^{i\theta_{\mathbf{j}}}$; we take the phase to vary as $\theta_{\mathbf{j}} = k_p j_x$, implying the injection of pairs with a quasimomentum $\mathbf{k}_p = k_p \mathbf{e}_x$. For a realization based on a driven nonlinear medium, $\nu \propto \sqrt{I_p}$ where I_p is the power of the pump laser, and $k_p \mathbf{e}_x$ would be the quasimomentum of the pump laser photons. Note that a gauge transformation $\hat{a}_{\mathbf{j}}^\dagger = \hat{a}_{\mathbf{j}} \exp[i\phi_{\mathbf{j}}]$ would modify both pattern of phases $\phi_{\mathbf{i}\mathbf{j}}$ and $\theta_{\mathbf{j}}$.

When the laser is switched off, $\nu = 0$, and there is no disorder, $\omega_{\mathbf{j}} = \omega_0$, we have the well known Hofstadter model [35]. The band structure of a semi-infinite strip (extending to the lower-half 2D-plane) is shown in Fig. 2a. The continuous bulk band structure consists of four bands (one for each site in the magnetic unit cell). The top and bottom bands are flat Landau levels separated from the two central bands by topological band gaps. Because of the boundary, one finds inside each topological band gap an edge state (dark line). The net number of these edge states (the number weighted by the sign of their slope) is a topologically protected quantity which does not depend on the shape of the edge and can be calculated from the bulk Hamiltonian [36].

We now turn on the parametric driving such that the resulting Hamiltonian can exhibit instability. Our goal is twofold: we want the system to be unstable *only* if we have a boundary, and in this case, the dominant unstable Bogoliubov modes should be chiral excitations localized at the system's boundary. We do this by choosing the parametric drive parameters so that the only pairs of photons that can be created in an energy and quasimomentum conserving fashion correspond to edge state excitations of the original ($\nu = 0$) model. For concreteness, we will focus on exciting the edge mode in the lower topological band gap (dispersion $\varepsilon_E(k)$). In the lab frame, we will thus tune the pump photon frequency ω_p and quasimomentum k_p so that a single pump photon can be converted into two edge excitations with frequency $\omega_p/2$ and quasimomentum $k_p/2$. In the rotating frame we use to write our Hamiltonians, this requirement reduces to $\varepsilon_E(k_p/2) = 0$. If this resonance condition is met, an arbitrarily weak parametric drive ν will cause instability of the edge mode. The required tuning is shown in Fig. 2a.

Because of the approximately linear dispersion relation of the edge mode, the above tuning guarantees that the parametric driving can resonantly create a pair of edge mode photons having momenta $k_p/2 \pm \delta k$, see the hollow circles in Figure 2(b). Thus, even for a weak parametric drive amplitude, the edge state will exhibit instability over a range of quasimomenta near $k_p/2$ (corresponding to a finite bandwidth around $\omega_p/2$ in the lab frame), see Figure 2(c).

Conversely, the energies of two bulk excitations always

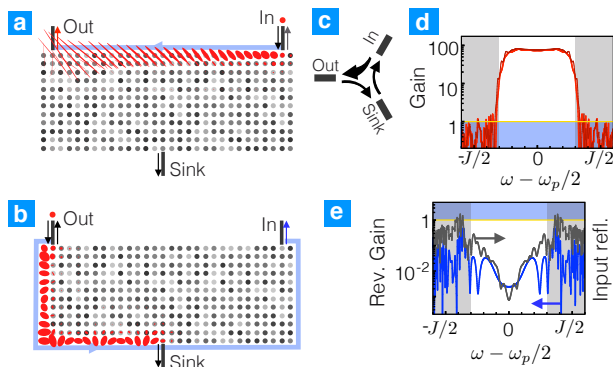


Figure 3. Linear response of the topological amplifier. (a-b) The topological amplifier is formed by a 30×12 array of photonic nanocavities. Three of the cavities at the edge of the sample are attached to waveguides, the input and output ports of the amplifier and an additional sink port. (c) The amplifier has the geometry of a circulator. (a-b) The red ellipses represent the linear response of the field inside the photonic array as a function of the incoming signal phase. The signal is injected at the port marked by an inward arrow. (a) A signal injected at the input port propagates unidirectionally toward the output port. The response is strongly phase sensitive, a signal with the right phase is amplified along the way. (d) Transmission power gain for the amplified quadrature as a function of the frequency of the input signal (counted off from half of the pump frequency) for a disordered (light thick line) and a clean sample (dark thin line). The reflection coefficient at the input is shown in panel (e) for the disordered sample. (b) A signal propagating from the output port toward the input port follows a different path and it is not amplified. Moreover, an appropriate matching of the impedances ensures that it leaks out at the sink port. The resulting (small) reverse transmission from the output to the input of the amplifier is the blue curve in panel (e). [Parameters: $\omega_0 = 2.14J$, $\Phi = \pi/2$, $\nu = 0.08J$, $k_p = 2.2$, $\kappa = 0.001J$, $\kappa_{\text{in}} = 2.6J$, $\kappa_{\text{out}} = 3J$, $\kappa_{\text{sink}} = 4.2J$. In the disordered simulations, the offset energies $\delta\omega_j$, represented by the greyscale in (a-b), are random numbers in the interval $-0.1J < \delta\omega_j < 0.1J$]

add up to a finite value, see Appendix B. In other words, all bulk parametric transitions have a finite detuning. This guarantees the bulk stability (even in the presence of disorder) for a driving amplitude ν below the minimal value of the bulk detuning.

III. TOPOLOGICAL NON-RECIPROCAL AMPLIFIER

Having shown how to realize an unstable topological edge mode, we now want to understand how one can use it. More precisely, we show that a finite size array of nanocavities coupled to simple waveguides can be used as a new kind of topologically-protected, phase-sensitive, quantum-limited amplifier. The role of the waveguides is two-fold: they serve as amplifier input-output ports and

they stabilize the dynamics.

We consider a realization of our system using a 30×12 array of nanocavities, and additionally include three coupling waveguides. Each waveguide is coupled to a site at the edge of the sample, as shown in Fig. 3a-b. This coupling is described using standard input/output theory, and is entirely characterized by the three rates κ_{in} , κ_{out} , and κ_{sink} , see Appendix C. In addition, we take each cavity to have an internal-loss decay rate κ .

When the small decay rate κ is neglected, and without parametric driving, the array can be operated as an ideal circulator where a signal from any waveguide is entirely transmitted into the next waveguide, see Figure 3c. Indeed, it is always possible to match the impedances at each port to cancel the back-reflection by tuning the corresponding coupling rate (κ_{in} , κ_{out} , or κ_{sink}). Once inside the array a wave in a topological band gap has no alternative but to chirally propagate along the edge. In addition, the impedance matching ensures that a wave impinging on a waveguide from the edge channel will be entirely transmitted.

We harness the robust non-reciprocity of this topological circulator to design an amplifier. We use the waveguide on the upper right (left) as input (output) port of the amplifier. We choose parametric driving parameters similar as in Fig. 2. In the finite geometry, the quasimomentum matching will be approximately realized only on the upper edge. Thus, the amplification occurs mainly in the region between the input and the output port.

The linear response of the amplifier is investigated numerically in Fig. 3. A signal injected into the array from the input port propagates chirally until it leaves the array through the output port, see Fig. 3a. Depending on its phase, it can be amplified or de-amplified along the way. Treating the amplifier as a phase-sensitive amplifier, we find that the power gain for the amplified signal quadrature is flat over a large bandwidth, corresponding to the frequency range over which the edge state dispersion is purely linear (see panel d). At the same time, any signals incident upon the output port will be almost entirely dumped into the sink port, and not reach the input port, see 3b. The residual reverse gain and input reflection are much smaller than unity, see panel e, ensuring the protection of a potentially fragile signal source (e.g. a qubit). Crucially, this strongly non-reciprocal amplifying behavior is of topological origin and is thus robust against disorder. We demonstrate this resilience by including moderate levels of disorder in our simulations (see Fig. 3).

Our numerical results are in qualitative agreement with analytical results for a model in which a 1D chiral edge state is coupled to three waveguides, see Appendix D. In this context, we find simple expressions for the impedance matching condition and the maximum power gain

$$\kappa_i = \frac{4v}{|u(j_y = -1)|^2}, \quad G \approx \exp\left[\frac{2\nu L}{v}\right],$$

respectively. Here, $u(j_y)$ is the transverse edge state wavefunction, v is the edge state velocity and L is the number of sites separating the input and the output ports. Thus, we see that the gain is the exponential of the rate 2ν of creation of down-converted pairs times the time of flight L/v from the input to the output port. While we have focused on operation as a phase-sensitive amplifier, for frequencies different from $\omega_p/2$, one could also use the device as a quantum-limited phase preserving (i.e. non-degenerate) amplifier.

Quantum-limited amplification

The noise floor of the amplifier is the frequency-resolved noise of the amplified output quadrature, see Appendix C. It is plotted in dark (light) red for a clean (disordered) sample in Fig. 4a. The quantum limit on a phase-sensitive amplifier is to have zero added noise, implying that the noise floor is simply set by the amplification of the vacuum fluctuations entering the input port. The added noise (expressed as an equivalent number of input quanta) is plotted in Fig. 4b; despite disorder and noise associated with internal loss, the amplifier is nearly quantum limited over the entire amplification bandwidth.

IV. TOPOLOGICAL STATIONARY STATE

Next, we investigate the quantum fluctuations in the stationary state that arise from the steady flow of photons from the parametric pump to the amplifier ports in the form of down-converted radiation. Physically, such a flow arises because vacuum fluctuations entering the input port (within the amplification bandwidth) are amplified inside the array before exiting through the output port. The resulting stationary state of each cavity is Gaussian, and can be represented by a Wigner function; these are visualized as a set of noise ellipses in Fig. 4c. Each noise ellipse completely characterizes the steady state of the corresponding site once all remaining sites and the waveguides have been traced out. The areas of the ellipses are constrained from below by the Heisenberg uncertainty principle and assume the minimal possible value for pure states. The bulk sites are all in the trivial quantum groundstate, which is characterized by circular ellipses with the minimal area and zero photons. On the other hand, the eccentricity, the area and the average on-site photon number (color code) grow while moving from the input to the output port along the upper edge (the major axis corresponds to the amplified quadrature). We emphasize that in a thermal equilibrium setting, the area of the ellipses would be equal on all sites and directly reflect the environment temperature. Here, the excess noise of the sites on the upper edge has a quantum origin. This phenomenon has been termed quantum heating [37–39].

Due to quantum heating, the stationary state of each cavity along the edge corresponds to a thermal squeezed

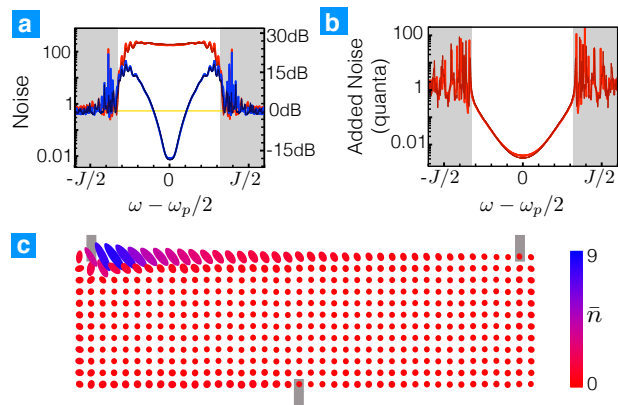


Figure 4. Quantum stationary state and noise properties of the topological amplifier. (a) Output noise spectra. The field leaking out of the output waveguide [top left corner in panel (c)] is strongly squeezed. Plotted are the noise spectral densities for both the amplified (red) and squeezed (blue) quadratures of the output field, for both a disordered (light thick lines) and a clean sample (dark thin lines). The noise in the amplified quadrature is only slightly larger than the standard quantum limit (i.e. the amplified vacuum noise from the input port). The excess noise (in quanta) for both a disordered and a clean sample is shown in panel (b). (c) Quantum noise ellipses of the field inside the amplifier. In the bulk, the ellipses have a circular shape and their area is as small as allowed by the Heisenberg principle, representing a standard vacuum state. In contrast, the ellipses at the edge are anisotropic and have areas larger than the shot noise level. This excess noise does not come from a finite temperature of the environment but rather by the amplification of the zero-point fluctuations (quantum heating). Plotted as a color code is also the average number of circulating photons on each site. The sites attached to waveguides are marked in grey. ([Parameters: 40×12 sites, $\omega_0 = 2.14J$, $\Phi = \pi/2$, $\nu = 0.08J$, $k_p = 2.2$, $\kappa = 0.001J$, $\kappa_{\text{in}} = 2.6J$, $\kappa_{\text{out}} = 3J$, $\kappa_{\text{sink}} = 4.2J$. For the disordered simulations the offset energies $\delta\omega_j$ are random numbers in the interval $-0.1J < \delta\omega_j < 0.1J$. For all plots, there is only vacuum noise entering from each waveguide.]

state, implying that the squeezed quadrature has a larger variance than required by the uncertainty principle. Nonetheless, the frequency-resolved output noise is strongly squeezed below the vacuum level (for frequencies within the amplification bandwidth). Remarkably, the quality of the output squeezing is not deteriorated in the presence of disorder. For the parameters considered here, more than 15dB of output squeezing are predicted both in the case of a clean and a disordered sample, see the blue curves in Fig. 4a.

V. IMPLEMENTATION

Photonic gauge fields have been already realized in several experimental platforms [7, 9, 10]. The only additional ingredient of our proposal is the parametric pumping with a finite quasimomentum. In the setup of Ref.

[10], one could fabricate the microrings from a nonlinear optical $\chi^{(2)}$ material and drive them with a single laser impinging at a finite angle. The implementation of parametric pumping [32] and synthetic gauge fields [13, 20, 22, 25, 32] is in principle possible in any cavity array platform where a nonlinear resource is available. These include photonic crystals microcavities [40] fabricated from nonlinear optical $\chi^{(2)}$ materials [41–43] or piezoelectric materials, optomechanical arrays based on optomechanical crystals [44, 45], or lattices of superconducting resonators with embedded Josephson nonlinearities [46]. We also note that very recently, a proposal for realizing topological insulator physics in a classical optical network with nonlinearities was put forward [47]; such a setup could also be adapted to implement our scheme, as it contains all the necessary ingredients.

VI. CONCLUSIONS AND OUTLOOK

In this work, we have introduced a means to tie the squeezing and amplification of vacuum fluctuations to topological properties of a band structure. Our work represents a new design principle for a non-reciprocal quantum-limited amplifier which has topological protection. Non-reciprocal amplifiers have the potential to revolutionize experiments with superconducting qubits, as they could eliminate the need for ferrite-based circulators and the accompanying insertion losses which limit current experiments. A variety of (non-topological) designs based on multiple parametric interactions have been proposed recently [48, 49] and even realized experimentally [50, 51], including a travelling wave parametric amplifier (TWPA) built using an array of over 2000 Josephson junctions [52]. In such a conventional TWPA, the reverse transmission is at best unity, and even small amounts of disorder can lead to large amounts of unwanted reflection gain. In contrast, the topological underpinnings of our design ensure reverse transmission and input reflection coefficients that are well below unity even in the presence of disorder.

More generally, our topological amplifier differs markedly from other proposed topological devices such as isolators or non-amplifying circulators [6], in that it has some protection against internal losses: in the large gain limit, only the loss (and corresponding noise) in the immediate vicinity of the input port hinder quantum limited operations, as it is only this noise which is amplified to any significant degree (see Appendix E for a quantitative discussion of this point).

In conclusion, our work shows how utilizing the topological properties of an unstable bosonic Hamiltonian provides a new route for both engineering electromagnetic vacuum fluctuations, and correspondingly, constructing a new kind of topologically-protected, non-reciprocal quantum amplifier. It opens the door to future studies, both pursuing other kinds of novel applications, as well as more fundamental issues (e.g. the effects of

additional photon-photon interactions in such systems).

ACKNOWLEDGEMENTS

V.P., C.B., and F.M. acknowledge support by an ERC Starting Grant OPTOMECH, by the DARPA project ORCHID, and by the European Marie-Curie ITN network cQOM. M.H. and A.A.C. acknowledge support from NSERC. We thank Ignacio Cirac, Sebastian Huber, and André Xuereb for discussion.

Appendix A: Generalized normal mode decomposition

We consider the generic Hamiltonian Eq. (2). We group all ladder operators with quasimomentum \mathbf{k} in a vector of ladder operators, $|\hat{\mathbf{a}}_{\mathbf{k}}\rangle = (\hat{a}_{\mathbf{k},1}, \dots, \hat{a}_{\mathbf{k},N}, \hat{a}_{\mathbf{k}_p-\mathbf{k},1}^\dagger, \dots, \hat{a}_{\mathbf{k}_p-\mathbf{k},N}^\dagger)^T$. The Heisenberg equation of motion for $|\hat{\mathbf{a}}_{\mathbf{k}}\rangle$ reads

$$\frac{d}{dt}|\hat{\mathbf{a}}_{\mathbf{k}}\rangle = -i\sigma_z h_{\mathbf{k}}|\hat{\mathbf{a}}_{\mathbf{k}}\rangle, \quad (\text{A1})$$

where

$$\sigma_z = \begin{pmatrix} \mathbb{1}_N & 0 \\ 0 & -\mathbb{1}_N \end{pmatrix}$$

and $h_{\mathbf{k}}$ is the Bogoliubov de Gennes Hamiltonian

$$h_{\mathbf{k}} = \begin{pmatrix} \mu_{\mathbf{k}} & i\nu_{\mathbf{k}} \\ -i\nu_{\mathbf{k}}^\dagger & \mu_{\mathbf{k}_p-\mathbf{k}} \end{pmatrix}.$$

In the following, we explicitly construct a complete set of Bogoliubov operators $\hat{\beta}_{n,\mathbf{k}}$, leading to the generalized normal mode decomposition Eq. (3), from the solutions of the eigenvalue problem

$$\sigma_z h_{\mathbf{k}}|\mathbf{k}_{n,l}\rangle = \Lambda_{\mathbf{k},n,l}|\mathbf{k}_{n,l}\rangle. \quad (\text{A2})$$

We note that we need to find only N annihilation operators while the eigenvalue problem has dimension $2N$. However, the equations for quasimomentum $\mathbf{k}_p - \mathbf{k}$ are not independent from the equations for quasimomentum \mathbf{k} . The ones can be obtained from the others by taking the adjoint. This doubling of the degrees of freedom accompanied by an embedded particle-hole symmetry occurs because we are effectively applying a single-particle formalism to a problem where the number of excitations is not conserved.

From Eq. (A2) it is easy to prove that eigenvalues which are not related by complex conjugation $\Lambda_{n,l,\mathbf{k}} \neq \Lambda_{n',l',\mathbf{k}}^*$ have σ_z -orthogonal eigenvectors, $\langle \mathbf{k}_{n,l} | \sigma_z | \mathbf{k}_{n',l'} \rangle = 0$. Moreover, the eigenvectors with real eigenvalues have a non-zero symplectic norm, $\langle \mathbf{k}_{n,l} | \sigma_z | \mathbf{k}_{n,l} \rangle \neq 0$ (which can also be negative). We assign the label $l = +$ to the positive norm eigenvectors.

We construct a set of orthonormal Bogoliubov creation operators from these positive norm solutions with the definition,

$$\hat{\beta}_{n,\mathbf{k}} \equiv \langle \mathbf{k}_{n,+} | \sigma_z | \hat{a}_{\mathbf{k}} \rangle. \quad (\text{A3})$$

We note that the scalar product between a standard vector and a vector of operators is an operator. Moreover, we have to normalize the positive vectors $|\mathbf{k}_{n,l}\rangle$ according to $\langle \mathbf{k}_{n,+} | \sigma_z | \mathbf{k}_{n,+} \rangle = 1$ such that $[\hat{\beta}_{n,\mathbf{k}}, \hat{\beta}_{n',\mathbf{k}}^\dagger] = \delta_{nn'}$. By taking the time derivative of Eq. (A3) and plugging Eq. (A1) and the adjoint of Eq. (A2) we immediately find

$$\dot{\hat{\beta}}_{n,\mathbf{k}} = -i \langle \mathbf{k}_{n,+} | \sigma_z \sigma_z h_{\mathbf{k}} | \hat{a}_{\mathbf{k}} \rangle = -i \Lambda_{n,+,\mathbf{k}} \hat{\beta}_{n,\mathbf{k}}$$

Thus, $\hat{\beta}_{n,\mathbf{k}}$ is the annihilation operator of a harmonic oscillator with energy $E_{n,\mathbf{k}} = \Lambda_{n,+,\mathbf{k}}$. In the same way, one could construct a set of creation operators $\hat{\beta}_{n,\mathbf{k}_p-\mathbf{k}}^\dagger$ from the negative norm eigenvectors $|\mathbf{k}_{n,-}\rangle$. However, it is possible to focus only on the positive norm solutions because of the particle-hole symmetry: the information encoded in the negative norm solutions $|\mathbf{k}_{n,-}\rangle$ is also encoded in the positive norm solutions $|\mathbf{k}_p - \mathbf{k}_{n,+}\rangle$.

The remaining eigenvectors have zero norm, $\langle \mathbf{k}_{n,\pm} | \sigma_z | \mathbf{k}_{n,\pm} \rangle = 0$. They appear whenever the Hamiltonian is unstable. In this case, the matrix $\sigma_z h_{\mathbf{k}}$ has pairs of complex conjugated eigenvalues $\Lambda_{n,+,\mathbf{k}} = \Lambda_{n,-,\mathbf{k}}^*$. For concreteness, we indicate with the label + the eigenvalues with positive imaginary part. The pair of eigenvectors $|\mathbf{k}_{n,\pm}\rangle$ are not orthogonal to each other, $\langle \mathbf{k}_{n,+} | \sigma_z | \mathbf{k}_{n,-} \rangle \neq 0$. In this case, we define a pair of commuting ladder operators as,

$$\hat{\beta}_{n,\mathbf{k}} \equiv \frac{1}{\sqrt{2}} (\langle \mathbf{k}_{n,-} | + i \langle \mathbf{k}_{n,+} |) \sigma_z | \hat{a}_{\mathbf{k}} \rangle, \quad (\text{A4})$$

$$\hat{\beta}_{n,\mathbf{k}_p-\mathbf{k}}^\dagger \equiv \frac{1}{\sqrt{2}} (\langle \mathbf{k}_{n,-} | - i \langle \mathbf{k}_{n,+} |) \sigma_z | \hat{a}_{\mathbf{k}} \rangle. \quad (\text{A5})$$

The bosonic commutation relations are recovered by requiring the normalization $\langle \mathbf{k}_{n,-} | \sigma_z | \mathbf{k}_{n,+} \rangle = i$. By taking the time derivative of Eq. (A4) and using Eq. (A1), the transpose of Eq. (A2), and Eq. (A5) we find

$$\dot{\hat{\beta}}_{n,\mathbf{k}} = -i \text{Re}[\Lambda_{n,+,\mathbf{k}}] \hat{\beta}_{n,\mathbf{k}} + \text{Im}[\Lambda_{n,+,\mathbf{k}}] \hat{\beta}_{n,\mathbf{k}_p-\mathbf{k}}^\dagger.$$

Likewise, we find

$$\dot{\hat{\beta}}_{n,\mathbf{k}_p-\mathbf{k}}^\dagger = -i \text{Re}[\Lambda_{n,+,\mathbf{k}}] \hat{\beta}_{n,\mathbf{k}_p-\mathbf{k}}^\dagger + \text{Im}[\Lambda_{n,+,\mathbf{k}}] \hat{\beta}_{n,\mathbf{k}}.$$

The corresponding Hamiltonian is the two-mode squeezing Hamiltonian (Eq.(4)) with energies $E_{n,\mathbf{k}} = -E_{n,\mathbf{k}_p-\mathbf{k}} = \text{Re}[\Lambda_{n,+,\mathbf{k}}]$ and amplification amplitude $\lambda_{n,\mathbf{k}} = \text{Im}[\Lambda_{n,+,\mathbf{k}}]$.

When the matrix $\sigma_z h$ is diagonalizable, the set of Bogoliubov annihilation operators defined in Eqs. (A3) and (A4) is complete. The pathological case where the matrix $\sigma_z h$ is not diagonalizable occurs only exactly at the threshold of an instability.

Appendix B: Details of the calculation of the band structure

Stability of the bulk Hamiltonian

In the main text, we have explained that a bosonic Hamiltonian with anomalous pairing terms is unstable when it allows the creation of a pair of Bogoliubov excitations without any net energy change. In other words, the sum of two quasiparticle energies should be zero. We have also claimed that for the parameters of Figure 2 the bulk Hamiltonian is stable because no combination of bulk states whose energies add up to zero exists. This is not immediately obvious from the plot of the standard band structure. In order to visually illustrate the absence of such combination of bulk states one has rather to plot the corresponding Bogoliubov de Gennes band structure, see Fig. 5. For each value of k_x , the latter is formed by both the quasiparticle energies E_{n,k_x} (blue bands) as well as the energies $-E_{n,k_p-k_x}$ (grey bands). In analogy to the descriptions of quasiparticles in fermionic superconductors, one refers to the former (latter) as the particle (the hole) bands of the system. The absence of crossings between particle and hole bands for the chosen pump laser frequency implies that there is no combination of a pair of bulk quasiparticles whose energies add up to zero while at the same time the corresponding quasimomenta add up to k_p . In the limit of vanishing parametric driving ($\nu = 0$), the minimal distance between particle and hole bands is the minimal detuning of a parametric transition involving two bulk states.

In the presence of weak disorder, there is no selection rule for the quasimomenta of the pair of quasiparticles created in a parametric transition. Nevertheless, all possible parametric transitions are still detuned because the band gap separating particle and hole bands is not merely locally defined (for a fixed k_x) but rather extends to the whole Brillouin zone. Thus, the stability of the bulk Hamiltonian is a robust feature.

As explained in Appendix A, the Bogoliubov de Gennes band structure can be calculated by diagonalizing the matrix $\sigma_z h(k_x)$ where $h(k_x)$ is the first-quantized Bogoliubov de Gennes Hamiltonian equivalent to the second quantized Hamiltonian Eq. (5) of the main text in the presence of periodic boundary conditions both in the x - and y - directions.

Band structure of a strip

Figure 2 of the main text represents the band structure and the amplification amplitudes of a semi-infinite strip. Those have been derived from the the Bogoliubov de Gennes band structure and the amplification rates of a strip with two physical edges as explained below.

We have simulated a finite strip of width $M = 40$ magnetic unit cells. For each value of the quasimomentum k_x , the set of energies E_{n,k_x} and $-E_{n,k_p-k_x}$ forming the

BdG band structure and the corresponding amplification rates $\lambda_n(k_x)$ are calculated by diagonalizing the relevant $4M \times 4M$ matrix $\sigma_z h(k_x)$. While strictly speaking the energy spectrum is discrete, the spacing between subsequent bulk states is not visible on the figure scale. The resulting band structure [panels (b-c)] and the corresponding amplification rates [panel (d)] are shown in Fig. 5. By inspecting the corresponding wavefunctions one can easily distinguish between particle and hole bands (plotted in blue and grey, respectively), edge and bulk states (plotted by the thick dark and thin light lines, respectively) and upper- and lower-edge states (solid and dashed lines, respectively).

Since the hole bands are not independent from the particle bands and refer to the same set of normal modes, we have not displayed the hole energies in the plots in the main text. Moreover, we have shown only the edge states localized on the upper edge. Removing the edge states localized on the lower edge effectively corresponds to plotting the band structure of a semi-infinite strip extending to the lower half plane.

We note that the particle (hole) edge states cross the hole (particle) band. Thus, a pair formed by an edge and a bulk excitation can in principle also be resonantly excited. However, the corresponding matrix element is very small and the resulting amplification rate is not visible on the scale of the figure.

Analytical derivation of Edge state dispersion and amplification rate

Here, we outline a direct derivation of the edge state dispersion for a semi-infinite strip.

We first, consider the case where the parametric driving is switched off ($\nu = 0$). The Hamiltonian in terms of the annihilation operators \hat{a}_{j_y, k_x} of a plane wave with quasimomentum k_x on the $|j_y|$ -th row reads

$$\hat{H} = \sum_{j_y, k_x} (\omega_0 - 2J \cos(k_x + \pi j_y/2)) \hat{a}_{j_y, k_x}^\dagger \hat{a}_{j_y, k_x} - J \left(\hat{a}_{j_y-1, k_x}^\dagger \hat{a}_{j_y, k_x} + \hat{a}_{j_y, k_x}^\dagger \hat{a}_{j_y-1, k_x} \right). \quad (\text{B1})$$

Since, the strip extends to the lower-half plane the j_y -th sum runs over the negative integers. By definition of the normal modes $\hat{\alpha}_{n, k_x}$ and eigenenergies $E_n[k_x]$ we have $\hat{H} = \sum_{n, k_x} E_n[k_x] \hat{\alpha}_{n, k_x}^\dagger \hat{\alpha}_{n, k_x}$, or equivalently $[\hat{\alpha}_{n, k_x}, \hat{H}] = E_n[k_x] \hat{\alpha}_{n, k_x}$. By plugging the ansatz $\hat{\alpha}_{n, k_x}^\dagger = \sum_{j_y} u_{n, k_x}[j_y] \hat{a}_{j_y, k_x}^\dagger$, we arrive to the first-quantized time-independent Schrödinger equation which we set in the matrix form,

$$\begin{pmatrix} u_{n, k_x}[j_y - 1] \\ u_{n, k_x}[j_y] \end{pmatrix} = \tilde{M}_{j_y}(\epsilon_n[k_x]) \begin{pmatrix} u_{n, k_x}[j_y] \\ u_{n, k_x}[j_y + 1] \end{pmatrix} \\ = \begin{pmatrix} -\epsilon_n[k_x] - 2 \cos(k_x + \pi j_y/2) & -1 \\ 1 & 0 \end{pmatrix} \begin{pmatrix} u_{n, k_x}[j_y] \\ u_{n, k_x}[j_y + 1] \end{pmatrix}. \quad (\text{B2})$$

Here, we have defined $\epsilon_n[k_x] = (E_n[k_x] - \omega_0)/J$. In principle, the above equation holds only for $j_y \leq -2$ but not for $j_y = -1$ because there is no row corresponding to $j_y = 0$. One can circumvent this problem by formally adding the row $j_y = 0$ together with the boundary condition $u_{n, k_x}[0] = 0$. Thus, one immediately finds

$$\begin{pmatrix} u_{n, k_x}[j_y] \\ u_{n, k_x}[j_y - 1] \end{pmatrix} = \prod_{|j'_y| < |j_y|} \tilde{M}_{j'_y}(\epsilon_n[k_x]) \begin{pmatrix} u_{n, k_x}[-1] \\ 0 \end{pmatrix}. \quad (\text{B3})$$

Next, we focus on the edge state solutions. In the following, we drop the subscript n because there is only one edge state in each band gap, see below. For the edge states we have to enforce the boundary condition

$$\lim_{j_y \rightarrow -\infty} u_{k_x}[j_y] = 0 \quad (\text{B4})$$

Equivalently, one can require

$$\lim_{m \rightarrow \infty} \begin{pmatrix} u_{k_x}[-4m - 1] \\ u_{k_x}[-4m] \end{pmatrix} = \lim_{m \rightarrow \infty} (M(\epsilon[k_x]))^m \begin{pmatrix} u_{k_x}[-1] \\ 0 \end{pmatrix} = 0. \quad (\text{B5})$$

where $M(\epsilon[k_x])$ is the transfer matrix by a full magnetic unit cell (four sites),

$$M(\epsilon[k_x]) = \tilde{M}_{-4}(\epsilon[k_x]) \tilde{M}_{-3}(\epsilon[k_x]) \tilde{M}_{-2}(\epsilon[k_x]) \tilde{M}_{-1}(\epsilon[k_x]). \quad (\text{B6})$$

(5) is fulfilled if and only if the vector $(1, 0)$ is an eigenvector of the 4-site transfer matrix $M(\epsilon[k_x])$ whose eigenvalue has modulus smaller than unity. In other words, the edge state dispersion is determined by the conditions,

$$\begin{aligned} M_{2,1}(\epsilon[k_x]) &= -\epsilon(-4 + \epsilon^2 + 2 \cos[2k_x]) \\ &\quad + 2 \cos[k_x](\epsilon^2 - 4 \sin[k_x]^2) = 0, \quad (\text{B7}) \\ |M_{1,1}(\epsilon[k_x])| &= |\epsilon^4 - 7\epsilon^2 - 2\epsilon(\cos[k_x] + \sin[k_x]) \\ &\quad + 3 + 2 \sin[2k_x] - 4 \cos[4k_x]| < 1. \end{aligned}$$

Equation (6) is a third order polynomial in the dimensionless energy ϵ . Thus, it has three roots for each value of k_x . Each root corresponds to a solution inside one of the three band gaps (lower, middle, or upper). By plugging the analytical expression of each root of Equation (6) into Equation (7) we find the range of k_x where the corresponding edge state is defined: the interval $-\pi < k_x < 0$ for the upper edge state, $0 < k_x < \pi$ for the lower edge state, and the two intervals $-\pi/2 < k_x < 0$ and $\pi/2 < k_x < \pi$ for the edge state in the local band gap between the two central bands. In order to enforce the bosonic commutation relations $[\hat{\alpha}_{k_x}, \hat{\alpha}_{k_x}^\dagger] = 1$, we have to appropriately normalize the single-particle wavefunctions $\sum_{j_y} |u_{k_x}[j_y]|^2 = 1$. This condition fixes the modulus of the wavefunction on the initial site $u_{k_x}[-1]$. The complex phase of $u_{k_x}[-1]$ is arbitrary. For concreteness, we choose $u_{k_x}[-1]$ to be real.

Next, we show how the edge state is modified by the parametric pump. The pump drive written in terms of the annihilation operators \hat{a}_{j_y, k_x} reads,

$$\hat{H}_{\text{pump}} = i\frac{\nu}{2} \sum_{j_y, k_x} \left(\hat{a}_{j_y, k_x}^\dagger \hat{a}_{j_y, k_p - k_x}^\dagger - \hat{a}_{j_y, k_x} \hat{a}_{j_y, k_p - k_x} \right). \quad (\text{B8})$$

Before pursuing an exact numerical solution we adopt a semi-analytical treatment. We focus on the lower band gap edge state which is resonantly driven for the parameters of Fig. 2 of the main text. As in the main text, we consider the case where the frequency and quasimomentum of the pump laser are chosen to resonantly excite pair of edge photons with quasimomentum $k_p/2$,

$$\omega_0 = -J\varepsilon[k_p/2]. \quad (\text{B9})$$

In this case, it is convenient to introduce the quasimomentum $\delta k = k_x - k_p/2$ counted off from $k_p/2$. By rewriting the full Hamiltonian (including the pump) in terms of the edge states ladder operators $\hat{\alpha}_{\delta k}$ and keeping only the terms that acts on the lower edge state (we neglect an off-resonant parametric coupling to the bulk modes and the other edge states), we find $H^{(\text{edge})} = \sum_{\delta k} H_{\delta k}^{(\text{edge})}/2$

$$\begin{aligned} H_{\delta k}^{(\text{edge})} &= \tilde{E}_n(\delta k) (\hat{\alpha}_{\delta k}^\dagger \hat{\alpha}_{\delta k} - \hat{\alpha}_{-\delta k}^\dagger \hat{\alpha}_{-\delta k}) \\ &+ \Delta[\delta k] (\hat{\alpha}_{\delta k}^\dagger \hat{\alpha}_{\delta k} + \hat{\alpha}_{-\delta k}^\dagger \hat{\alpha}_{-\delta k}) \\ &+ iV[\delta k] (\hat{\alpha}_{\delta k}^\dagger \hat{\alpha}_{-\delta k}^\dagger - \hat{\alpha}_{\delta k} \hat{\alpha}_{-\delta k}). \end{aligned} \quad (\text{B10})$$

Here, we have grouped all excitation conserving terms into two contributions whose amplitudes $\tilde{E}_n(\delta k)$ and $\Delta_n(\delta k)$ are an odd an even function of δk , respectively,

$$\tilde{E}_n(\delta k) = J \sum_{n \geq 1} \frac{d^{2n-1} \varepsilon}{dk_x^{2n-1}} \Big|_{k_p/2} \frac{\delta k^{2n-1}}{(2n-1)!} \quad (\text{B11})$$

$$\Delta(\delta k) = J \sum_{n \geq 1} \frac{d^{2n} \varepsilon}{dk_x^{2n}} \Big|_{k_p/2} \frac{\delta k^{2n}}{(2n)!}. \quad (\text{B12})$$

Note that $\Delta(\delta k)$ is the quasimomentum dependent detuning of the parametric transition creating pairs of photons with quasimomentum $k_p/2 \pm \delta k$. The corresponding parametric coupling is given by

$$V(\delta k) = \nu \sum_{j_y} u_{\delta k}[j_y] u_{-\delta k}[j_y]. \quad (\text{B13})$$

It is easy to show that it can be expanded in terms of even powers of δk and that the leading order is ν

$$V(\delta k) = \nu - \sum_{n \geq 1} \nu_n \delta k^{2n}. \quad (\text{B14})$$

The edge state is unstable over the finite quasimomentum interval where $V(\delta k) > |\Delta(\delta k)|$. Following the general procedure presented in Appendix A, we find the eigenenergies and amplification amplitude of the Bogoliubov edge state normal modes

$$E(\delta k) = \tilde{E}(\delta k), \quad \lambda(\delta k) = \sqrt{V(\delta k)^2 - \Delta(\delta k)^2}. \quad (\text{B15})$$

and

$$E(\delta k) = \tilde{E}(\delta k) + \sqrt{\Delta(\delta k)^2 - V(\delta k)^2}. \quad (\text{B16})$$

in the unstable and stable quasimomentum ranges, respectively.

We can recover the edge state dispersion and lineshape of the amplification amplitude obtained numerically and shown in Fig 2 of the main text by keeping the leading order contributions in Eqs. (B11, B12, B14),

$$V(\delta k) \approx \nu - \nu_1 \delta k^2 \quad \nu_1 = 0.014, \quad (\text{B17})$$

$$\tilde{E}(\delta k) \approx v \delta k, \quad \frac{v}{J} = \frac{d\varepsilon}{dk_x} \Big|_{k_p/2} = -1, \quad (\text{B18})$$

$$\Delta(\delta k) \approx J \frac{d^2 \varepsilon}{dk_x^2} \Big|_{k_p/2} \frac{\delta k^2}{2}, \quad \frac{d^2 \varepsilon}{dk_x^2} \Big|_{k_p/2} = 1.4. \quad (\text{B19})$$

Appendix C: Input-output formalism

We include the effects of dissipation using the standard input-output formalism [1]. Each site is described by the Langevin equation

$$\dot{\hat{a}}_{\mathbf{j}} = i[\hat{H}, \hat{a}_{\mathbf{j}}] - \kappa_{\mathbf{j}} \hat{a}_{\mathbf{j}}/2 + \sqrt{\kappa_{\mathbf{j}}} \hat{a}_{\mathbf{j}}^{(\text{in})}. \quad (\text{C1})$$

Here, $\kappa_{\mathbf{j}}$ is the decay rate on site \mathbf{j} . On the sites coupled to waveguides, the decay rates κ_{in} , κ_{out} , and κ_{sink} are induced by the coupling to the waveguides and are chosen to achieve impedance matching. In this case, the input fields $\hat{a}_{\mathbf{j}}^{(\text{in})}$ describe the field impinging on site \mathbf{j} from the corresponding waveguide including the field vacuum fluctuations. The field $\hat{a}_{\mathbf{j}}^{(\text{out})}$ leaking out of the waveguide is given by the input-output relations

$$\hat{a}_{\mathbf{j}}^{(\text{out})} = \hat{a}_{\mathbf{j}}^{(\text{in})} - \sqrt{\kappa_{\mathbf{j}}} \hat{a}_{\mathbf{j}}. \quad (\text{C2})$$

On the remaining sites (i.e. those not coupled to waveguides), we assume a small uniform decay rate κ ($\kappa_{\mathbf{j}} = \kappa$) corresponding to internal loss; $\hat{a}_{\mathbf{j}}^{(\text{in})}$ describes the corresponding incident vacuum fluctuations associated with this loss port.

The linear response and the noise properties of the array are simple functions of the retarded Green's functions

$$\tilde{G}_E(\omega, \mathbf{j}, \mathbf{j}') = -i \int_{-\infty}^{\infty} dt \Theta(t) e^{i\omega t} \langle [\hat{a}_{\mathbf{j}}(t), \hat{a}_{\mathbf{j}'}^\dagger(0)] \rangle, \quad (\text{C3})$$

$$\tilde{G}_I(\omega, \mathbf{j}, \mathbf{j}') = -i \int_{-\infty}^{\infty} dt \Theta(t) e^{i\omega t} \langle [\hat{a}_{\mathbf{j}}^\dagger(t), \hat{a}_{\mathbf{j}'}(0)] \rangle. \quad (\text{C4})$$

We calculate the above Green's functions numerically for a finite array.

Response Ellipses

In Fig. 3a (Fig. 3b) we show the linear response of the pair of quadratures

$$\begin{aligned}\hat{X}_{\mathbf{j}} &= \frac{1}{\sqrt{2}} \left(e^{i\theta_{\mathbf{j}}/2} \hat{a}_{\mathbf{j}}^{\dagger}(t) + e^{-i\theta_{\mathbf{j}}/2} \hat{a}_{\mathbf{j}}(t) \right), \\ \hat{Y}_{\mathbf{j}} &= \frac{i}{\sqrt{2}} \left(e^{i\theta_{\mathbf{j}}/2} \hat{a}_{\mathbf{j}}^{\dagger}(t) - e^{-i\theta_{\mathbf{j}}/2} \hat{a}_{\mathbf{j}}(t) \right).\end{aligned}\quad (\text{C5})$$

to a classical field of frequency $\omega_p/2$ injected at the input (output) port as a function of the field phase ϑ ,

$$\langle \hat{a}_{\mathbf{j}'}^{(in)} \rangle = \sqrt{\kappa_{\mathbf{j}'}} e^{i\vartheta},$$

\mathbf{j}' indicates the site attached to the relevant injection waveguide ($\mathbf{j}' = \mathbf{j}_{in}$ for Fig. 3a, $\mathbf{j}' = \mathbf{j}_{out}$ for Fig. 3b). The response on each site is represented by the ellipse

$$\begin{pmatrix} \langle \hat{X}_{\mathbf{j}} \rangle \\ \langle \hat{Y}_{\mathbf{j}} \rangle \end{pmatrix} = \begin{pmatrix} \cos \gamma_{\mathbf{j}\mathbf{j}'} & -\sin \gamma_{\mathbf{j}\mathbf{j}'} \\ \sin \gamma_{\mathbf{j}\mathbf{j}'} & \cos \gamma_{\mathbf{j}\mathbf{j}'} \end{pmatrix} \begin{pmatrix} r_{\mathbf{j}\mathbf{j}'}^+ \cos(\vartheta - \eta_{\mathbf{j}\mathbf{j}'}) \\ r_{\mathbf{j}\mathbf{j}'}^- \sin(\vartheta - \eta_{\mathbf{j}\mathbf{j}'}) \end{pmatrix},$$

where

$$r_{\mathbf{j}\mathbf{j}'}^{\pm} = \kappa_{\mathbf{j}'} \left(|\tilde{G}_E(0, \mathbf{j}, \mathbf{j}')| \pm |\tilde{G}_I(0, \mathbf{j}, \mathbf{j}')| \right)$$

are the major and minor semiaxes of the ellipse, and

$$\gamma_{\mathbf{j}\mathbf{j}'} = \arg \left(\frac{G_E(0, \mathbf{j}, \mathbf{j}')}{G_I(0, \mathbf{j}, \mathbf{j}')} \right) / 2 - \theta_{\mathbf{j}}/2 \quad (\text{C6})$$

is the angle parametrizing the orientation of the major semiaxis. In the figure, the reference angle $\gamma_{\mathbf{j}\mathbf{j}'} = 0$ is rotated by $\pi/2$ compared to the page vertical. The maximum (minimum) response $r_{\mathbf{j}\mathbf{j}'}^+$ ($r_{\mathbf{j}\mathbf{j}'}^-$) at site \mathbf{j} to an input field at the port \mathbf{j}' is obtained for the driving phase $\vartheta = \eta_{\mathbf{j}\mathbf{j}'}$ ($\vartheta = \eta_{\mathbf{j}\mathbf{j}'} + \pi/2$),

$$\eta_{\mathbf{j}\mathbf{j}'} = \pi/2 - \arg \left(G_E(0, \mathbf{j}, \mathbf{j}') G_I(0, \mathbf{j}, \mathbf{j}') \right) / 2. \quad (\text{C7})$$

Gain, Reverse Gain, and Input Reflection

As we analyze our amplifier in the phase-sensitive mode of operation, it is useful to consider its scattering properties in a quadrature representation, using an optimal quadrature basis fields in the input and output waveguides. The relevant scattering between these waveguides is described by

$$\begin{aligned}\hat{\mathcal{X}}_{out}[\omega] &= s_{\mathcal{X},\mathcal{U}}[\omega] \hat{\mathcal{U}}_{in}[\omega] + s_{\mathcal{X},\mathcal{V}}[\omega] \hat{\mathcal{V}}_{in}[\omega] + \dots \\ \hat{\mathcal{Y}}_{out}[\omega] &= s_{\mathcal{Y},\mathcal{U}}[\omega] \hat{\mathcal{U}}_{in}[\omega] + s_{\mathcal{Y},\mathcal{V}}[\omega] \hat{\mathcal{V}}_{in}[\omega] + \dots\end{aligned}$$

where we have omitted writing terms describing contributions from vacuum noise incident from the internal loss ports, as well as terms describing the reflection of noise

incident from the output waveguide (due to slightly imperfect impedance matching). We define the quadratures of the output waveguide as

$$\begin{aligned}\hat{\mathcal{X}}_{out}(t) &= \frac{1}{\sqrt{2}} \left(e^{i\theta_{out}} \hat{a}_{\mathbf{j}_{out}}^{(out)\dagger}(t) + e^{-i\theta_{out}} \hat{a}_{\mathbf{j}_{out}}^{(out)}(t) \right), \\ \hat{\mathcal{Y}}_{out}(t) &= \frac{i}{\sqrt{2}} \left(e^{i\theta_{out}} \hat{a}_{\mathbf{j}_{out}}^{(out)\dagger}(t) - e^{-i\theta_{out}} \hat{a}_{\mathbf{j}_{out}}^{(out)}(t) \right).\end{aligned}$$

while the quadratures of the input-waveguide are defined as

$$\begin{aligned}\hat{\mathcal{U}}_{in}(t) &= \frac{1}{\sqrt{2}} \left(e^{i\theta_{in}} \hat{a}_{\mathbf{j}_{in}}^{(in)\dagger}(t) + e^{-i\theta_{in}} \hat{a}_{\mathbf{j}_{in}}^{(in)}(t) \right), \\ \hat{\mathcal{V}}_{in}(t) &= \frac{i}{\sqrt{2}} \left(e^{i\theta_{in}} \hat{a}_{\mathbf{j}_{in}}^{(in)\dagger}(t) - e^{-i\theta_{in}} \hat{a}_{\mathbf{j}_{in}}^{(in)}(t) \right).\end{aligned}$$

We will define both the quadrature basis in each coupling waveguide so that $|s_{\mathcal{X},\mathcal{U}}[\omega = 0]|$ is maximal. This implies that the largest amplification of a narrow-band signal centered at zero frequency ($\omega_p/2$ in the lab frame) occurs when the incident signal is in the $\hat{\mathcal{U}}_{in}$ quadrature of the input waveguide, with the amplified output being contained in the output field $\hat{\mathcal{X}}_{out}$ quadrature of the output waveguide. It also follows naturally that for vacuum noise inputs, $\hat{\mathcal{Y}}_{out}$ will be the optimally squeezed quadrature. An explicit calculation of the scattering matrix in terms of the Green's functions introduced above shows that the angles defining these preferred input and output quadratures are given by

$$\theta_{in} = \eta_{\mathbf{j}_{out}\mathbf{j}_{in}}, \quad \theta_{out} = \gamma_{\mathbf{j}_{out}\mathbf{j}_{in}} + \theta_{\mathbf{j}_{out}}/2, \quad (\text{C8})$$

see Eqs. (C6,C7). The fact that in general $\theta_{in} \neq \theta_{out}$ is a simple reflection of the fact that our system can both perform phase-sensitive amplification of incident signals, as well as simply rotate incident signals in phase space.

The frequency dependent power gain is then by definition given by the transmission probability:

$$\begin{aligned}G(\omega) &= |s_{\mathcal{X},\mathcal{U}}(\omega)|^2 \\ &= \kappa_{in} \kappa_{out} \left| e^{i(\theta_{in} - \theta_{out})} G_E(\omega, \mathbf{j}^{(out)}, \mathbf{j}^{(in)}) \right. \\ &\quad + e^{i(\theta_{in} + \theta_{out})} G_I(\omega, \mathbf{j}^{(out)}, \mathbf{j}^{(in)}) \\ &\quad + e^{i(\theta_{out} - \theta_{in})} G_E^*(-\omega, \mathbf{j}^{(out)}, \mathbf{j}^{(in)}) \\ &\quad \left. + e^{-i(\theta_{in} + \theta_{out})} G_I^*(-\omega, \mathbf{j}^{(out)}, \mathbf{j}^{(in)}) \right|^2 / 4\end{aligned}$$

The reverse gain is obtained similarly by exchanging the two indices of the Green's functions in the above formula and in Eq. (C8). Finally, the input reflection probability describes the reflection of signals incident in the (ampli-

fied) \mathcal{U} quadrature of the input port

$$R[\omega] = |s_{\mathcal{U},\mathcal{U}}(\omega)|^2 \left(\left| e^{i\theta_{\text{in}}} \left(1 - i\kappa_{\text{in}} G_E(\omega, \mathbf{j}^{(\text{out})}, \mathbf{j}^{(\text{in})}) \right) + e^{-i\theta_{\text{in}}} \left(1 + i\kappa_{\text{in}} G_I^*(-\omega, \mathbf{j}^{(\text{out})}, \mathbf{j}^{(\text{in})}) \right) \right| + \left| e^{i\theta_{\text{in}}} \left(1 - i\kappa_{\text{in}} G_I(\omega, \mathbf{j}^{(\text{out})}, \mathbf{j}^{(\text{in})}) \right) + e^{-i\theta_{\text{in}}} \left(1 + i\kappa_{\text{in}} G_E^*(-\omega, \mathbf{j}^{(\text{out})}, \mathbf{j}^{(\text{in})}) \right) \right| \right)^2 / 4.$$

Added noise and squeezing

The symmetrized frequency-resolved noise in the amplified and de-amplified output-waveguide output field quadratures shown in Figure 4(a) are defined as

$$S_{\mathcal{X},\mathcal{X}}(\omega) = \int_{-\infty}^{\infty} \frac{dt}{2} e^{i\omega t} \left\{ \hat{\mathcal{X}}_{\text{out}}(t), \hat{\mathcal{X}}_{\text{out}}(0) \right\},$$

$$S_{\mathcal{Y},\mathcal{Y}}(\omega) = \int_{-\infty}^{\infty} \frac{dt}{2} e^{i\omega t} \left\{ \hat{\mathcal{Y}}_{\text{out}}(t), \hat{\mathcal{Y}}_{\text{out}}(0) \right\},$$

respectively. The number of added noise quanta shown in Figure 4(b) is defined by,

$$S_{\text{add}}(\omega) \equiv \frac{S_{\mathcal{X},\mathcal{X}}(\omega)}{G(\omega)} - \frac{1}{2}.$$

Noise Ellipses

In Figure 4(c), the stationary state of each site \mathbf{j} is represented as a noise ellipse. The noise ellipse on a particular site \mathbf{j} is obtained by diagonalizing the corresponding covariance matrix

$$V_{\mathbf{j}} = \begin{pmatrix} \langle \hat{X}_{\mathbf{j}}^2 \rangle & \langle \hat{X}_{\mathbf{j}} \hat{Y}_{\mathbf{j}} + \hat{Y}_{\mathbf{j}} \hat{X}_{\mathbf{j}} \rangle \\ \langle \hat{X}_{\mathbf{j}} \hat{Y}_{\mathbf{j}} + \hat{Y}_{\mathbf{j}} \hat{X}_{\mathbf{j}} \rangle & \langle \hat{Y}_{\mathbf{j}}^2 \rangle \end{pmatrix} = \begin{pmatrix} \cos \tilde{\gamma}_{\mathbf{j}} & \sin \tilde{\gamma}_{\mathbf{j}} \\ -\sin \tilde{\gamma}_{\mathbf{j}} & \cos \tilde{\gamma}_{\mathbf{j}} \end{pmatrix} \begin{pmatrix} (\tilde{r}_{\mathbf{j}}^+)^2 & 0 \\ 0 & (\tilde{r}_{\mathbf{j}}^-)^2 \end{pmatrix} \begin{pmatrix} \cos \tilde{\gamma}_{\mathbf{j}} & -\sin \tilde{\gamma}_{\mathbf{j}} \\ \sin \tilde{\gamma}_{\mathbf{j}} & \cos \tilde{\gamma}_{\mathbf{j}} \end{pmatrix},$$

and identifying the square root of its eigenvalues $\tilde{r}_{\mathbf{j}}^+$ and $\tilde{r}_{\mathbf{j}}^-$ as the ellipse semi-axes and the angle $\tilde{\gamma}_{\mathbf{j}}$ as the ellipse rotation angle (the reference angle $\tilde{\gamma}_{\mathbf{j}} = 0$ is rotated by $\pi/2$ compared to the page vertical).

Appendix D: Effective model for the edge state coupled to waveguides

In this supplementary note we want to derive an effective quantum field theory for the edge state coupled to a waveguide. We want to model a finite system which will then support a single edge state with a ring geometry (i.e. periodic boundary conditions). We adopt the

simplest possible approach valid when the input signal has a bandwidth well within the amplifier bandwidth. In this case, we can approximate the edge state velocity and amplification rates to be constant, $E \approx v\delta k$, $\Delta \approx 0$, and $V(\delta k) \approx \nu$, respectively. Moreover, we can neglect the quasimomentum dependence of the edge state transverse wavefunction. We thus arrive at the edge state ladder operator

$$\hat{c}(j_{\parallel}) = \sqrt{\frac{1}{N}} \sum_{n=1}^N e^{i\delta k_n j_{\parallel}} \hat{\alpha}_{\delta k} \approx e^{-i\kappa_p j_{\parallel}/2} \sum_{j_{\perp}} u[j_{\perp}] \hat{a}_{j_{\parallel}, j_{\perp}}, \quad (\text{D1})$$

where N is the number of sites along the edge, and the indexes j_{\parallel} and j_{\perp} ($j_{\perp} \geq 1$) label the position in the directions parallel and longitudinal to the edges (for the edge state along the upper edge described above $j_{\parallel} = j_x$ and $j_{\perp} = -j_y$). Moreover, $u(j_{\perp})$ is the transverse edge state wavefunction, $u(j_{\perp}) \equiv u_{k_p/2}(-j_{\perp})$ see Eqs. (B3,B7). The periodic boundary conditions $\hat{c}(j_{\parallel}) = \hat{c}(N + j_{\parallel})$ are enforced by the quasimomentum quantization $\delta k_n = 2\pi n/N$.

We consider a waveguide attached to a single site along the edge in the longitudinal position $j_{\parallel} \equiv j_{\text{ex}}$. The coupling to the waveguide as described by standard input-output theory is entirely characterized by the decay rate κ . Since, the edge state is the only state within the amplifier bandwidth the coupling of the waveguide to a single site is equivalent to a direct coupling to the edge state at the same longitudinal position j_{ex} with the renormalized decay rate $\kappa' = \kappa |u[j_{\perp} = 1]|^2$. The resulting Langevin equation reads

$$\dot{\hat{c}}(j_{\parallel}) = i[\hat{H}^{(\text{edge})}, \hat{c}(j_{\parallel})] - \frac{\kappa'}{2} \delta_{j_{\parallel}, j_{\text{ex}}} \hat{c}(j_{\parallel}) + \sqrt{\kappa'} \delta_{j_{\parallel}, j_{\text{ex}}} \hat{a}^{(\text{in})}, \quad (\text{D2})$$

with the input-output relations

$$\hat{a}^{(\text{out})} = \hat{a}^{(\text{in})} - \sqrt{\kappa'} \hat{c}(j_{\text{ex}}) \quad (\text{D3})$$

Next we take the continuum limit by defining the chiral edge field

$$\hat{c}(z) = \sqrt{\frac{1}{L}} \sum_{n=-\infty}^{\infty} e^{i\delta k_n j_{\parallel}} \hat{\alpha}_{\delta k}, \quad (\text{D4})$$

where L is the edge length and the periodic boundary conditions $\hat{c}(z) = \hat{c}(z + L)$ follow from the quasimomentum quantization $\delta k_n = 2\pi n/L$. From Eq. (B10) with $\hat{E} = v\delta k$, $\Delta = 0$, and $V(\delta k) = \nu$, and Eq. (D2) we find the field equations

$$(\partial_t + v\partial_z) \hat{c}(z) = \nu \hat{c}^\dagger(z) - \frac{\kappa'}{2} \delta(z - z_{\text{ex}}) \hat{c}(z) + \sqrt{\kappa'} \delta(z - z_{\text{ex}}) \hat{a}^{(\text{in})}. \quad (\text{D5})$$

We note that due to the point-interaction with the waveguide the field $\hat{c}(z)$ is not continuous at the position $z = z_{\text{ex}}$ where the waveguide is attached, $\hat{c}(z_{\text{ex}} + 0_+) \neq \hat{c}(z_{\text{ex}} + 0_-)$

(0_+ and 0_- are infinitesimal positive and negative numbers, respectively). Keeping this in mind, the input output relation in the continuous limit reads

$$\hat{a}^{(\text{out})} = \hat{a}^{(\text{in})} - \sqrt{\kappa'}(\hat{c}(0_+) + \hat{c}(0_-))/2. \quad (\text{D6})$$

Before investigating the interaction with the waveguide, we first discuss the propagation inside the ring. For concreteness we consider $v > 0$ such that $\hat{c}(z_{\text{ex}} + 0_+)$ ($\hat{c}(z_{\text{ex}} + 0_-)$) is the field immediately after (before) the interaction with the waveguide. A signal travels an almost complete round trip from $z = z_{\text{ex}} + 0_+$ to $z = L + z_{\text{ex}} + 0_+ = z_{\text{ex}} + 0_-$ in the time $t = L/v$. During this time no interaction with the waveguide takes place. From Eq. (D5), one readily finds

$$\begin{aligned} \hat{X}(z_{\text{ex}} + 0_-, L/v + t_0) &= e^{\nu L/v} \hat{X}(z_{\text{ex}} + 0_+, t_0), \\ \hat{Y}(z_{\text{ex}} + 0_-, L/v + t_0) &= e^{-\nu L/|v|} \hat{Y}(z_{\text{ex}} + 0_+, t_0). \end{aligned}$$

Here, we have introduced the amplified and de-amplified quadratures, $\hat{X} = (\hat{c}^\dagger + \hat{c})/\sqrt{2}$ and $\hat{Y} = i(\hat{c}^\dagger - \hat{c})/\sqrt{2}$. We can conclude that a signal with the right phase during a complete round trip inside the ring experience a power gain

$$G = e^{2\nu L/v}. \quad (\text{D7})$$

Next, we discuss the interaction with the waveguide. An input signal from the waveguide will be partly reflected and partly transmitted into the ring at $z = 0_+$. Then, it will propagate inside the ring until it has completed a round trip. A signal with the right phase will be amplified along the way. Before starting a new round trip, part of the amplified signal returns into the waveguide. If the signal remaining in the ring at the beginning of the second round trip is smaller compared to the signal in the ring at the beginning of the first round trip, the signal will decay after few round trips. In this regime, the waveguide stabilizes the edge state. By integrating the Heisenberg equations (D5) close to $z = 0$ we find

$$\begin{pmatrix} \sqrt{|v|}\hat{c}(0_+) \\ \hat{a}^{(\text{out})} \end{pmatrix} = \begin{pmatrix} r & t \\ -t & r \end{pmatrix} \begin{pmatrix} \sqrt{|v|}\hat{c}(0_-) \\ \hat{a}^{(\text{in})} \end{pmatrix} \quad (\text{D8})$$

where r and t are the reflection and transmission probability amplitudes,

$$r = \frac{4 - g^2}{4 + g^2}, \quad t = \frac{4g}{4 + g^2}, \quad g = \sqrt{\frac{\kappa'}{v}}. \quad (\text{D9})$$

To prevent instability, we require that the transmission t be large enough that the field in the edge-mode ring does not grow with each round trip. The simplest case is where we tune the decay rate κ so that all of the incident wave in the edge mode ends up in the coupling waveguide, i.e. $r = 0$, $t = 1$. This requires $g = 2$, or in terms of the decay rate κ , the edge state velocity v , and the edge state transversal wavefunction at the edge $u(j_\perp = 1)$, we find

$$\kappa = \frac{4v}{|u(j_\perp = 1)|^2}. \quad (\text{D10})$$

If this impedance matching condition is met, signals incident from the waveguide in the \hat{X} quadrature will be reflected back with a power gain $G = G_{\text{Max}}$ independent of frequency. The impedance matching ensures that multiple traversals of the ring are impossible, which both precludes instability, but also prevents the formation of standing wave resonances and a strongly frequency-dependent gain.

We note that the effective model described above can be straightforwardly extended to describe a chiral edge state coupled to several waveguides. In particular, we consider a set up with two impedance matched waveguides at position $z = z_{\text{in}}$ and $z = z_{\text{out}}$ ($z_{\text{out}} - z_{\text{in}} = L$), respectively. A signal from the first waveguide entering the edge state at position $z = z_{\text{in}}$ is entirely transmitted into the second waveguide at position $z = z_{\text{out}}$. For the appropriate phase of the input signal, we have

$$\hat{U}^{\text{in}}(t) = \sqrt{v}\hat{X}(z_{\text{in}} + 0_+, t), \quad (\text{D11})$$

where $\hat{U}^{(\text{in})}$ is the input quadrature. We denote \hat{X}^{out} , the corresponding amplified quadrature at $z = z_{\text{out}}$,

$$\hat{X}^{\text{out}}(t) = -\sqrt{v}\hat{X}(z_{\text{out}} + 0_-, t). \quad (\text{D12})$$

From Eq. (D5) one finds

$$|\hat{X}^{\text{out}}(t + L/v)|^2 = G|\hat{U}^{\text{out}}(t)|^2 \quad (\text{D13})$$

where the gain G is given by Eq. (D7).

Comparison between finite size simulations and effective model

In the regime where our effective theory applies (for signals well within the amplifier bandwidth), it can reproduce well the simulations of finite arrays. There are some quantitative differences due to well understood finite size effects. For instance, the edge state velocity is not constant in the finite size array but rather decreases close to the edges where the edge state propagation changes direction. For this reason the gain does not depend only on the number of sites separating the input and the output port but also on the precise position of the ports. We have placed the input and output port close to the edges to enhance the gain. Indeed, the gain in the finite size simulations is slightly larger than predicted by Eq. (D7). Due to the position dependent edge state velocity also the value of the decay rate required to obtain impedance matching depends on the position where the waveguide is attached (and is lower at the edges).

We note that the analytic continuum model can be extended to capture the frequency dependence of the gain and noise of our travelling wave amplifier; one needs however to incorporate into the model the leading-order quasimomentum dependence of the edge state velocity (which creates an effective pump detuning for the relevant parametric process). This will be presented in a future work.

Appendix E: Quantitative analysis of the resilience of the topological amplifier to losses

Here, we show that our quantum amplifier design offers some degree of resilience to intrinsic losses and the corresponding noise. We want to calculate noise which is added to a signal propagating from the input to the output port when intrinsic losses are present. In addition to the impedance matched outcoupling towards the waveguides at the input and output ports, we consider a loss channel on each site and denote the corresponding decay rate as $\kappa_j^{(\text{loss})}(z)$.

In the continuous limit, and with the same approximations as above, we find the quantum field equations valid in the region between the input and output port

$$(\partial_t + v\partial_z)\hat{X}(z, t) = (\nu - \kappa^{(\text{loss})}(z)/2)\hat{X}(z, t) - \sqrt{\kappa^{(\text{loss})}(z)}\hat{X}^{(\text{loss})}(z, t). \quad (\text{E1})$$

where $\hat{X}^{(\text{loss})}(z, t)$ is the vacuum noise: $\langle \hat{X}^{(\text{loss})}(z, t) \rangle = 0$ and

$$\langle \hat{X}^{(\text{loss})}(z, t)\hat{X}^{(\text{loss})}(z', t') \rangle = \frac{1}{2}\delta(z - z')\delta(t - t'). \quad (\text{E2})$$

We Fourier transform into frequency space and find the solution

$$\begin{aligned} \hat{X}[z, \omega] &= e^{[(i\omega + \nu)(z - z_{\text{in}}) - \int_{z_{\text{in}}}^z \kappa^{(\text{loss})}(z')dz'/2]/v} \hat{X}(z_{\text{in}} + 0_+, \omega) \\ &+ \frac{1}{v} \int_{z_{\text{in}}}^z dz' e^{[(i\omega + \nu)(z - z') - \int_{z'}^z \kappa^{(\text{loss})}(z'')dz''/2]/v} \\ &\times \sqrt{\kappa^{(\text{loss})}(z')}\hat{X}^{(\text{loss})}(z', \omega). \end{aligned} \quad (\text{E3})$$

Putting together Eq. (E3) for $z = z_{\text{out}} - 0_-$ with Eqs. (D11, D12) we can relate the output signal \hat{X}^{out} to the input signal \hat{U}^{in} of the amplifier

$$\begin{aligned} \hat{X}^{\text{out}}[\omega] &= -e^{[(i\omega + \nu)L - \int_{z_{\text{in}}}^{z_{\text{out}}} \kappa^{(\text{loss})}(z')dz'/2]/v} \hat{U}^{\text{in}}[\omega] \\ &+ \frac{1}{\sqrt{v}} \int_{z_{\text{in}}}^{z_{\text{out}}} dz' e^{[(i\omega + \nu)(z_{\text{out}} - z') - \int_{z'}^{z_{\text{out}}} \kappa^{(\text{loss})}(z'')dz''/2]/v} \\ &\times \sqrt{\kappa^{(\text{loss})}(z')}\hat{X}^{(\text{loss})}(z', \omega). \end{aligned} \quad (\text{E4})$$

The added noise $S_{\text{add}}(\omega)$ in noise quanta is by definition,

$$S_{\text{add}}(\omega) = \frac{S_{\mathcal{X}, \mathcal{X}}(\omega)}{G(\omega)} - \frac{1}{2}. \quad (\text{E5})$$

where $S_{\mathcal{X}, \mathcal{X}}(\omega)$ is the symmetrized noise at the output port,

$$S_{\mathcal{X}, \mathcal{X}}[\omega]\delta(\omega + \omega') = \frac{1}{2}\langle \{\hat{\mathcal{X}}[\omega], \hat{\mathcal{X}}[\omega']\} \rangle. \quad (\text{E6})$$

and $G(\omega)$ is the gain. We note that in our simple approach $S_{\mathcal{X}, \mathcal{X}}$, G and S_{add} are frequency independent. From Eqs. (E4, E2) we find

$$G = e^{[2\nu L - \int_{z_{\text{in}}}^{z_{\text{out}}} \kappa^{(\text{loss})}(z')dz']/v} \quad (\text{E7})$$

and

$$S_{\text{add}} = \frac{1}{v} \int_0^L dr e^{-[2\nu r - \int_0^L \kappa^{(\text{loss})}(r + z_{\text{in}})dr']/v} \kappa^{(\text{loss})}(r + z_{\text{in}}). \quad (\text{E8})$$

From this expression we see that for $2\nu > \kappa^{(\text{loss})}(z)$ the noise added at position $r + z_{\text{in}}$ is cut off exponentially as a function of the distance r from the input. In particular, in the large gain limit and assuming that $\kappa^{(\text{loss})}(z)$ is smooth close to $z = z_{\text{in}}$, we can approximate

$$S_{\text{add}} \approx \frac{\kappa^{(\text{loss})}(z_{\text{in}})}{2\nu}. \quad (\text{E9})$$

Note crucially that as one increases the length L of the amplifying channel, the gain increases exponentially, while the added noise remains constant. We thus see explicitly that the amplifying channel is immune to the majority of the internal loss noise in the system.

-
- [1] C. C. Gerry and P. L. Knight. *Introductory Quantum Optics*. Cambridge University Press, 2005.
- [2] Carlton M. Caves. Quantum-mechanical noise in an interferometer. *Phys. Rev. D*, 23:1693–1708, 1981.
- [3] Bernard Yurke, Samuel McCall, and John Klauder. SU(2) and SU(1,1) interferometers. *Phys. Rev. A*, 33(6):4033–4054, 1986.
- [4] Vittorio Giovannetti, Seth Lloyd, and Lorenzo Maccone. Quantum-enhanced measurements: Beating the standard quantum limit. *Science*, 306(5700):1330–1336, 2004.
- [5] D. J. Thouless, M. Kohmoto, M. P. Nightingale, and M. den Nijs. Quantized hall conductance in a two-

dimensional periodic potential. *Phys. Rev. Lett.*, 49:405–408, 1982.

- [6] Ling Lu, John D. Joannopoulos, and Marin Soljacic. Topological photonics. *Nat Photon*, 8(11):821–829, 2014.
- [7] Zheng Wang, Yidong Chong, J. D. Joannopoulos, and Marin Soljacic. Observation of unidirectional backscattering-immune topological electromagnetic states. *Nature*, 461(7265):772–775, 2009.
- [8] Takuya Kitagawa, Matthew A. Broome, Alessandro Fedrizzi, Mark S. Rudner, Erez Berg, Ivan Kassal, Alan Aspuru-Guzik, Eugene Demler, and Andrew G. White. Observation of topologically protected bound states in

- photonic quantum walks. *Nat Commun*, 3:882–, 2012.
- [9] Mikael C Rechtsman, Julia M Zeuner, Yonatan Plotnik, Yaakov Lumer, Daniel Podolsky, Felix Dreisow, Stefan Nolte, Mordechai Segev, and Alexander Szameit. Photonic Floquet topological insulators. *Nature*, 496(7444):196–200, 2013.
- [10] M. Hafezi, S. Mittal, J. Fan, A. Migdall, and J. M. Taylor. Imaging topological edge states in silicon photonics. *Nature Photonics*, 7(12):1001–1005, 2013.
- [11] Emil Prodan and Camelia Prodan. Topological phonon modes and their role in dynamic instability of microtubules. *Phys. Rev. Lett.*, 103:248101, 2009.
- [12] C. L. Kane and T. C. Lubensky. Topological boundary modes in isostatic lattices. *Nature Phys.*, 10(1):39–45, 2013.
- [13] V. Peano, C. Brendel, M. Schmidt, and F. Marquardt. Topological phases of sound and light. *Phys. Rev. X*, 5:031011, 2015.
- [14] Zhaoju Yang, Fei Gao, Xihang Shi, Xiao Lin, Zhen Gao, Yidong Chong, and Baile Zhang. Topological acoustics. *Phys. Rev. Lett.*, 114:114301, 2015.
- [15] Jayson Paulose, Bryan Gin-gu Chen, and Vincenzo Vitelli. Topological modes bound to dislocations in mechanical metamaterials. *Nature Phys.*, 11(2):153–156, 2015.
- [16] Roman Süssstrunk and Sebastian D. Huber. Observation of phononic helical edge states in a mechanical topological insulator. *Science*, 349(6243):47–50, 2015.
- [17] Lisa M. Nash, Dustin Kleckner, Alismari Read, Vincenzo Vitelli, Ari M. Turner, and William T. M. Irvine. Topological mechanics of gyroscopic metamaterials. *Proceedings of the National Academy of Sciences*, 112(47):14495–14500, 2015.
- [18] F D M Haldane and S Raghu. Possible Realization of Directional Optical Waveguides in Photonic Crystals with Broken Time-Reversal Symmetry. *Phys. Rev. Lett.*, 100(1):013904, 2008.
- [19] S. Raghu and F. D. M. Haldane. Analogs of quantum-hall-effect edge states in photonic crystals. *Phys. Rev. A*, 78:033834, 2008.
- [20] Jens Koch, Andrew A Houck, Karyn Le Hur, and S M Girvin. Time-reversal-symmetry breaking in circuit-QED-based photon lattices. *Phys. Rev. A*, 82(4):043811, 2010.
- [21] R. O. Umucalılar and I. Carusotto. Artificial gauge field for photons in coupled cavity arrays. *Phys. Rev. A*, 84:043804, 2011.
- [22] Kejie Fang, Zongfu Yu, and Shanhui Fan. Realizing effective magnetic field for photons by controlling the phase of dynamic modulation. *Nature Photon.*, 6(11):782–787, 2012.
- [23] Alexandru Petrescu, Andrew A Houck, and Karyn Le Hur. Anomalous Hall effects of light and chiral edge modes on the Kagomé lattice. *Phys. Rev. A*, 86(5):053804, 2012.
- [24] L. D. Tzuan, K. Fang, P. Nussenzeig, S. Fan, and M. Lipson. Non-reciprocal phase shift induced by an effective magnetic flux for light. *Nature Photonics*, 8:701–705, 2014.
- [25] M. Schmidt, S. Kessler, V. Peano, O. Painter, and F. Marquardt. Optomechanical creation of magnetic fields for photons on a lattice. *Optica*, 2(7):635–641, 2015.
- [26] Mohammad Hafezi, Eugene A Demler, Mikhail D Lukin, and Jacob M Taylor. Robust optical delay lines with topological protection. *Nature Phys.*, 7(11):907–912, 2011.
- [27] Alexander B. Khanikaev, S. Hossein Mousavi, Wang-Kong Tse, Mehdi Kargarian, Allan H. MacDonald, and Gennady Shvets. Photonic topological insulators. *Nature Mat.*, 12(3):233–239, 2012.
- [28] S. Mittal, J. Fan, S. Faez, A. Migdall, J. M. Taylor, and M. Hafezi. Topologically robust transport of photons in a synthetic gauge field. *Phys. Rev. Lett.*, 113:087403, 2014.
- [29] Ryuichi Shindou, Ryo Matsumoto, Shuichi Murakami, and Jun-ichiro Ohe. Topological chiral magnonic edge mode in a magnonic crystal. *Phys. Rev. B*, 87(17):174427, 2013.
- [30] G. Engelhardt and T. Brandes. Topological bogoliubov excitations in inversion-symmetric systems of interacting bosons. *Phys. Rev. A*, 91:053621, 2015.
- [31] Charles-Edouard Bardyn, Torsten Barzig, Gil Refael, and Timothy C. H. Liew. Chiral bogoliubov excitations in nonlinear bosonic systems. *Phys. Rev. B*, 93:020502, 2016.
- [32] Vittorio Peano, Martin Houde, Christian Brendel, Florian Marquardt, and Aashish A. Clerk. Topological phase transitions and chiral inelastic transport induced by the squeezing of light. *Nat Commun*, 7:–, 2016.
- [33] Ryan Barnett. Edge-state instabilities of bosons in a topological band. *Phys. Rev. A*, 88:063631, 2013.
- [34] Bogdan Galilo, Derek K. K. Lee, and Ryan Barnett. Selective population of edge states in a 2d topological band system. *Phys. Rev. Lett.*, 115:245302, 2015.
- [35] Douglas R. Hofstadter. Energy levels and wave functions of bloch electrons in rational and irrational magnetic fields. *Phys. Rev. B*, 14:2239–2249, 1976.
- [36] M. Z. Hasan and C. L. Kane. Colloquium: Topological insulators. *Rev. Mod. Phys.*, 82:3045–3067, 2010.
- [37] M. I. Dykman, M. Marthaler, and V. Peano. Quantum heating of a parametrically modulated oscillator: Spectral signatures. *Phys. Rev. A*, 83:052115, 2011.
- [38] V. Peano and M. Thorwart. Quasienergy description of the driven jaynes-cummings model. *Phys. Rev. B*, 82:155129, 2010.
- [39] Marc-Antoine Lemonde and Aashish A. Clerk. Real photons from vacuum fluctuations in optomechanics: The role of polariton interactions. *Phys. Rev. A*, 91:033836, 2015.
- [40] Masaya Notomi, Eiichi Kuramochi, and Takasumi Tanabe. Large-scale arrays of ultrahigh-q coupled nanocavities. *Nature Photon.*, 2(12):741–747, 2008.
- [41] S Mookherjea and A Yariv. Coupled resonator optical waveguides. *Ieee J Quantum Elect.*, 8(3):448, 2002.
- [42] B J Eggleton, B Luther-Davies, and K Richardson. Chalcogenide photonics. *Nat Photonics*, 5:141, 2011.
- [43] Jean Dahnah, Maria Pilar-Bernal, Nadège Courjal, Gwenn Ulliac, and Fadi Baida. Near-field observations of light confinement in a two dimensional lithium niobate photonic crystal cavity. *J. Appl. Phys.*, 110(7):074318, 2011.
- [44] Amir H Safavi-Naeini, Simon Gröblacher, Jeff T Hill, Jasper Chan, Markus Aspelmeyer, and Oskar Painter. Squeezed light from a silicon micromechanical resonator. *Nature*, 500(7461):185–189, 2013.
- [45] T P Purdy, P L Yu, R W Peterson, N S Kampel, and C A Regal. Strong Optomechanical Squeezing of Light. *Phys. Rev. X*, 3(3):031012, 2013.
- [46] D. L. Underwood, W. E. Shanks, Jens Koch, and A. A.

- Houck. Low-disorder microwave cavity lattices for quantum simulation with photons. *Phys. Rev. A*, 86:023837, 2012.
- [47] T. Shi, H. J. Kimble, and J. I. Cirac. Topological phenomena in classical optical networks. *arXiv:1603.03266v1*, 2016.
- [48] A. Metelmann and A. A. Clerk. Nonreciprocal Photon Transmission and Amplification via Reservoir Engineering. *Phys. Rev. X*, 5(2):021025, 2015.
- [49] Leonardo Ranzani and José Aumentado. Graph-based analysis of nonreciprocity in coupled-mode systems. *New J. Phys.*, 17(2):1–14, 2015.
- [50] Baleegh Abdo, Katrina Sliwa, S Shankar, Michael Hatridge, Luigi Frunzio, Robert Schoelkopf, and Michel Devoret. Josephson Directional Amplifier for Quantum Measurement of Superconducting Circuits. *Phys. Rev. Lett.*, 112(16):167701, 2014.
- [51] K M Sliwa, M Hatridge, A Narla, S Shankar, L Frunzio, R J Schoelkopf, and Michel Devoret. Reconfigurable Josephson Circulator/Directional Amplifier. *Phys. Rev. X*, 5(4):041020, 2015.
- [52] C Macklin, K O'Brien, D Hover, M E Schwartz, V Bolkhovskiy, X Zhang, W D Oliver, and I Siddiqi. A near-quantum-limited Josephson traveling-wave parametric amplifier. *Science*, 350(6258):307–310, 2015.

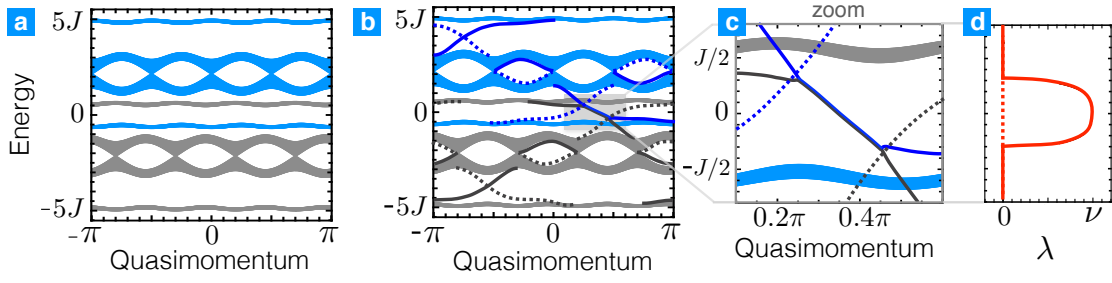


Figure 5. Bogoliubov de Gennes band structures. (a) BdG band structure for a system without boundaries. The stability of the bulk is protected by the complete band gaps separating neighboring particle and hole bands. (b-c) BdG band structure of a finite strip of width $M = 40$ magnetic unit cells. (d) Corresponding amplification amplitudes λ_n . The parameters are the same as for Figure 2 of the main text [$\omega_0 = 2.15J$, $\Phi = \pi/2$, $k_p = 2.2$, $\nu = 0.08J$.]